



Investigations on the capacitive behaviour of hydrothermally synthesised cadmium meta niobate incorporated reduced graphene oxide hybrid nanocomposite electrode material

M. Infant Shyam Kumar¹ and S. Shahil Kirupavathy^{1,2,*}

¹Department of Physics, Rajalakshmi Engineering College, Chennai 602105, India

²Department of Physics, Velammal Engineering College, Chennai 600066, India

Received: 8 July 2021

Accepted: 21 November 2021

Published online:
4 January 2022

© The Author(s), under exclusive licence to Springer Science+Business Media, LLC, part of Springer Nature 2021

ABSTRACT

Reduced graphene oxide/cadmium meta niobate (RGO/CN) hybrid nanocomposite was hydrothermally synthesised and subjected to structural characterization through X-ray diffraction and various microscopic analysis. Pure CN exhibited a cubical, rectangular slab like mixed morphology with average particle size ranging from 50 nm to 2 μm. Further, this work revealed that RGO/CN composite showed exfoliation of graphene sheets with mixed morphology of cubes and rectangular slab. Spectral analysis enabled in understanding the various functional groups present in RGO/CN. The optical band gap of prepared RGO/CN composite material was estimated as 4.024 eV. The calculated remanent polarization and coercive electric field of cadmium niobate (CN) and RGO/CN are $P_r = 0.0151 \mu\text{C cm}^{-2}$, $E_c = -1.30 \text{ kV cm}^{-1}$ and $P_r = 0.0685 \mu\text{C cm}^{-2}$, $E_c = -2.39 \text{ kV cm}^{-1}$, respectively. RGO/CN was developed into an electrode material and its electrochemical behaviour was evaluated by adopting the cyclic voltammetry and galvanostatic charging discharging measurements. The observed specific surface area of hybrid RGO/CN showed enhanced redox current rate than the pseudo-capacitive CN. Also, hybrid RGO/CN electrode furnished enhancement in specific capacitance for different scan rates and current density than CN. Specific capacitance of RGO/CN was estimated to be 58.2 F g^{-1} for very low molar H_2SO_4 electrolyte at a current density of 1 A g^{-1} . Furthermore, RGO/CN coated over carbon electrode furnished cyclic stability with 98% of capacitive retention after 500 cycles at 2 A g^{-1} . The maximum energy density of 8.08 Wh kg^{-1} with consuming high power density of 4137 W kg^{-1} at 1 A g^{-1} compared with few other reported materials make graphene nested CN nanocomposite stay as a significant material supporting energy storage applications.

Address correspondence to E-mail: shahilkirupavathy@yahoo.co.in

1 Introduction

In this technological world, researchers have considerable interest in developing flexible, bendable and wearable electronics, flat panel, power supplies and electronic displays using electrochemical supercapacitors. To build up these applications, electrodes are fabricated with preventive bending, folding and flexibility nature. Allotropes of carbon such as carbon nanotube, graphene and flexible carbon fibres are favourable agents for flexible energy storage devices owing to their excellent mechanical, electrochemical and electrical properties [1, 2]. Also, different forms of carbon materials such as graphene oxide (GO), RGO, functionalized reduced graphene oxide, carbon nanotubes, carbon aerogels and activated carbon have attracted much attention owing to its high-power density, very fast charging/discharging and excellent cycling stability.

Among the various carbon allotropes, reduced graphene oxide (RGO) is a 2-dimensional sheet comprising hybridized carbon sp² structure with different functional groups that can regulate its electrical, mechanical, optical, physical and chemical properties [3–6]. Graphene sheets stimulates the required surface area with irreversible agglomeration by developing strong π - π interaction and van der Waals force, which in turn results in high capacitive behaviour [1]. Moreover, the high surface area of graphene and its derivative's porous structure formation provides the short ion transport and diffusion distance, which is extremely recommended for high capacitive performance [7].

Graphene composed of hybrid coloumbites have been reported to be good performance electrode materials generating high electrochemical capacitance and exhibit high capacitance. Further, graphene-based hybrid composite electrode materials have been explored much with research interest on account of their collective and effective production of pseudo-capacitance and electrochemical double layer capacitor [8–10]. In addition, graphene-based composites are promising materials which exports many applications like energy storage sensors, water splitting, electrode fabrication in lithium batteries and biosensing applications. Also, its pseudo-capacitive nature is a highlighting property that can be used in supercapacitors, fuel cell devices and so on [11–14]. Nanocomposites when loaded with very low loading of graphene exhibits enhanced property in its

multifunctional aspects when compared to conventional materials and their composites [15]. Moreover, the lighter weight with simple processing makes it suitable for various cost-effective multifunctional applications.

Structural parameters of any hybrid material can be optimized and controlled during the synthesis. Various graphene-based composites have been synthesized using different synthesis routes such as electrochemical transformation, solvothermal, hydrogen reducing, hydrolysis process, solution precipitation and electrophoretic deposition, etc. Those described synthesis approach reported in various articles show that it is rather complex and difficult in controlling the compound structure [16–18]. The hydrothermal route adopted in this work is simpler, cost-effective and a fast synthesis route for synthesis of graphene-based hybrid composite structure for enhanced electrochemical performance. Also, this method stays as an excellent choice for preparing perovskite niobate and columbite niobate powders and its composites at low temperatures with minimal reaction time [19]. The degree of mixing and the reactivity of starting material by utilizing mixed solutions as reactants under high pressure can be done in the hydrothermal process. Owing to low temperature treatment, the grain size of the synthesized particles can be altered with multiple dimensions for improving various properties. Moreover, the loss of reaction species can be effectively prevented in this process when the reaction species is taken into a closed system.

The attraction towards the electrochemical performance reports such as specific capacitance, cycle stability, energy density and power density of columbite and perovskite materials are presented by many researchers [20–22]. To stimulate high performance in graphene-based electrochemical supercapacitors, focus is made on to graphene incorporated pseudocapacitive materials. This hybrid composite suppresses the restacking of graphene sheets and provides higher energy density, power density and promising pseudo-capacitance in the supercapacitor [23, 24].

Literature review reveal that niobate compounds have gathered much attention in the recent days due to their ferroelectric, piezoelectric, pyroelectric, electro-optical, photorefractive and photocatalytic properties [25–27]. However, the electrochemical oxidation and reduction property of niobates in

supercapacitors are not been assessed much [28]. Hence to bring out the good performance in compound making and also to increase thermal stability, RGO is incorporated with columbite cadmium meta niobate (CN) with molecular formula CdNb_2O_6 belonging to Pbcn space group.

This paper demonstrates the scalable synthesis of cost effective, porous, reduced graphene oxide/cadmium meta niobate (RGO/CN) electrode material by utilizing CN nano cubes with large specific surface area on to reduced graphene oxide by hydrothermal route. Furthermore, future implementation of RGO/CN as an electrode material for flexible supercapacitor is described through various characterization methods.

2 Preparation of nanocomposites

2.1 Materials

Graphite powder, KMnO_4 (99%), H_2SO_4 (98%), CdCO_3 (97%), Nb_2O_5 (99.95%), NaOH (97%), H_2O_2 (30% concentration), HCl (35% concentration) purchased from Sisco Research Laboratory (SRL), Maharashtra, India and Milli-Q water was used throughout the experiment. Various other chemicals, and solvents used for synthesis were of analytical grade and were used with no further purification.

2.2 Synthesis of graphene oxide (GO) and cadmium meta niobate (CN)

GO was prepared by Hummer's technique (modified version) as described by Daniela and co-workers [29]. Here 2.5 g of graphite flakes and 2.5 g of sodium nitrate were mixed in 60 ml of concentrated sulphuric acid. This reaction mixture was placed in an ice bath for 2 h with constant stirring. To this 8 g of KMnO_4 was added gradually by maintaining the temperature at 20 °C. Further, the ice bath was removed from the reaction set up and kept at room temperature with continuous stirring till it turned into a pasty state. The above reaction mixture was further diluted with 125 ml deionized (DI) water and the temperature was raised to 98 °C. Now, the color of mixture turned to brown. Finally, the above suspension was treated with 15 ml of H_2O_2 (30%) to terminate the reaction. The mixture turned yellow and this was then washed using DI water and 10%

diluted HCl and centrifuged at 6000 rpm to remove unwanted residues.

CN nanostructures were synthesized by adopting the hydrothermal method in which 0.345 g of CdCO_3 and 0.265 g of Nb_2O_5 were mixed in 2 M of alkaline solution (NaOH) and stirred continuously for 30 min. The obtained white coloured mixture was transferred onto a Teflon lined stainless-steel autoclave and was subjected for continuous stirring. The autoclave was later sealed and heated to 200 °C for 24 h by maintaining autogenous pressure. The temperature of resultant mixture was brought down to room temperature and HCl was added to the mixture and it was then centrifuged at a speed of 6000 rpm. The precipitate was then rinsed using deionized water followed by ethanol to eliminate the hydroxides. The formed pure white colloids were dried for 6 h at 80 °C. This powder was further subjected to sintering by heating for 6 h at 700 °C. The resultant mixture was pure and thermally strong CN.

2.3 Preparation of RGO/CN nanocomposite

The precursors, GO colloids (0.1 g) and CN powder (0.4 g) were well dispersed in 15 mL ethanol and 35 ml distilled water. The pH of the dispersant was increased above 12 by adding ammonia drop wise to the solution. This pH modified colloidal mixture was stirred continuously for about 30 min. Further this mixture was ultrasonicated for 30 min to make the particles uniformly dispersed. Thereafter the ultrasonicated solution was transferred onto an autoclave and subjected to 180 °C for 2 h under autogenous pressure. To remove the surface impurities, this product was washed in distilled water and later HCl was added to the mixture and it was then centrifuged at a speed of 6000 rpm. Later this resultant product was kept for 2 h at 80 °C for drying.

3 Structural analysis

3.1 Diffraction analysis using X-ray

Diffraction studies on as prepared GO, CN and RGO/CN were done with the help of Rigaku X-ray diffractometer using Cu K_α radiation ($\lambda = 1.5406 \text{ \AA}$) with 2θ angle in the range of 5° to 90°. PXRD pattern of GO, CN and RGO/CN are presented in Fig. 1a, b and c. As described in reported article [30] the

oxidation of graphite was confirmed through the diffraction peak observed at $2\theta = 11.5^\circ$ as seen in Fig. 1a. The broad diffraction peak identified from PXRD is due to amorphous carbon and the broad peak centred at $d_{(002)} = 42^\circ$ corresponds to un-oxidized graphite [31].

CN belongs to the orthorhombic system with Pbcn space group and has lattice parameters $a = 14.7825(1) \text{ \AA}$, $b = 5.84852(4) \text{ \AA}$, $c = 5.14444(3) \text{ \AA}$, $V = 444.767(5) \text{ \AA}^3$ [32]. The observed PXRD peaks in Fig. 1b are matched with JCPDS Card No: 38-1428. The appearance of an additional less intense peak at 15° in Fig. 1c corresponding to RGO/CN indicates the presence of unreduced GO content due to defect formation, lattice contraction and exfoliation mechanisms [33]. Also, the appearance of new peak at $2\theta = 24^\circ$ in Fig. 1c implies that RGO coexist with CN. Thus, the PXRD pattern of RGO/CN confirms that GO is reduced with CN.

Prominent peaks observed in Fig. 1b and c were assigned to calculate the crystallite size of CN and RGO/CN using the Debye–Scherrer formula [34] and the average estimated crystallite sizes were 67 nm and 73 nm, respectively.

3.2 Morphology and composition analysis

FEI Quanta FEG 200 coupled with EDAX was involved to study the morphology of CN and RGO/CN. The morphologies of CN and RGO/CN are presented in Fig. 2a and b. HRSEM image of CN shown in Fig. 2a reveals a wide size distribution of columbite crystallites. In addition, pure CN exhibit a cubical, rectangular slab like mixed morphology having the average particle size ranging from 50 nm to 2 μm . RGO/CN composite exhibit exfoliation of graphene sheets with mixed morphology of cubes and rectangular slab are revealed in Fig. 2b. Moreover, the relative content of CN decreases with increasing GO under hydrothermal treatment and is in agreement with the PXRD results. Also, RGO when intercalated with CN exhibit a typical mixed morphology of graphene sheets [30] and CN. Thus, from electron microscopy studies, the excellent cube-like and rectangular slab-like morphology is established.

The EDAX compositional analysis of CN and RGO/CN nanostructures are demonstrated in Fig. 2c and d. The elements of CN (Cd: 10.54 wt% Nb: 58.61 wt% O: 30.85 wt%) is appreciably indexed from

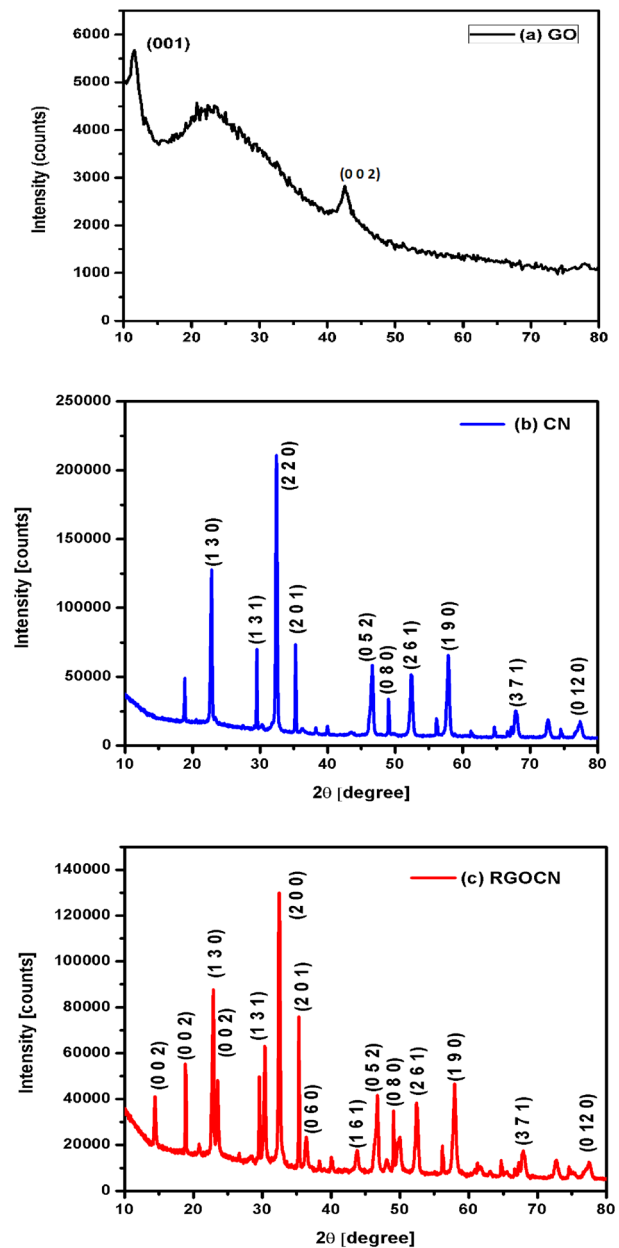


Fig. 1 X-ray diffraction pattern of **a** GO, **b** CN and **c** RGO/CN

Fig. 2c and that of RGO/CN elements are indexed from Fig. 2d as Cd: 5.12 wt% Nb: 7.46 wt% O: 12.56 wt% C: 74.86 wt%. Observed EDAX pattern confirms the homogeneity of carbon and CN elements. The distribution of different elements as observed in CN and RGO/CN are listed in Tables 1 and 2. This further establishes that RGO/CN exhibits mixed compositional behaviour.

3.3 High-resolution transmission electron microscopy (HRTEM) studies

High-resolution transmission electron microscopy (HRTEM) technique allows recording the images of the prepared materials at an atomic scale with ultimate resolution. A phase contrast is produced in the phase of the electron wave electron due to the change produced in the position of specimen and objective lens for the formation of image [35]. Transmission electron microscopy interfaced with high-resolution observation along with selected-area electron diffraction (SAED) was accomplished using the JEOL Model JEM-3010 system at 300 kV by fixing the powder sample on a microgrid.

The morphology and structural study on sample of GO, CN and RGO/CN were done using the HRTEM analysis. The HRTEM of GO shown in Fig. 3a clearly illustrates the high magnified image of flake-like structure in GO. Moreover, many layers of sheet-like GO of size ranging from ten to several nanometers were found wrinkled and folded together. SAED design of GO displayed in Fig. 3d shows the rings obtained due to diffraction. The unresolved dots formed by diffraction confirms that the GO flakes are amorphous [36]. The diffraction rings exhibited confirms the disorderliness in the GO nanosheets. The observed rings also give additional data about the interplanar distance d (100) for GO material and this was calculated as 7.4 Å using ImageJ software. This result is mapped with XRD analysis.

The HRTEM investigations for CN at high magnification shown in Fig. 3b, reveal cluster of CN nano cubes with 50 nm size. The corresponding SAED pattern analysed by choosing a specific area on CN nano cube illustrated in Fig. 3e indicates the existence of both bright diffraction spots and rings. The appearance of rings of these kinds indicates the polycrystalline structure of CN nano cube. The rings due to diffraction numbered from centre spot are designated to the (200), (201), (231), (261) and (133) planes whose interplanar distance are measured as 2.995 Å, 2.571 Å, 2.227 Å, 1.731 Å and 1.532 Å, respectively. The observed diffraction results are similar to that in XRD analysis [37, 38].

Figure 3c shows the HRTEM images of RGO/CN nanocomposite. In the composite structure, the CN nano cubes are dispensed thickly over the sheets of RGO. However, in certain regions, agglomeration of CN was noted on RGO surfaces. The composite size

of reduced graphene oxide encapsulated CN is nearly 500 nm. From the images it can be seen clearly that thin reduced graphene oxide layers are homogeneously deposited over CN mixed morphological structure. The corresponding diffraction rings are observed clearly from the SAED pattern of RGO/CN and is shown in Fig. 3f. In this figure we see five diffraction rings. These rings when counted from the centre spot are consigned to the (002), (131), (201), (231) and (202) planes and the measured interplanar distances are 4.42 Å, 3.12 Å, 2.53 Å, 2.25 Å and 1.99 Å, respectively. The shift in interplanar distance and diffraction plane found using Image J software when GO is reduced with CN and diffraction plane (002) with interplanar distance was approximately 0.442 nm. The appearance of the (002) diffraction line confirms the reduction of GO nanosheets and the restoration of ordered structure with CN [39]. The SAED pattern of RGO/CN also confirms the composite structure and is consistent with the XRD results.

4 Spectral analysis

4.1 FTIR spectral analysis

The different functional groups present in the prepared samples were examined in the wavelength ranging 4000–450 cm^{-1} using global and mercury source in a Perkin Elmer FT-IR equipment. FT-IR spectrum of GO shown in Fig. 4a represents the existence of hydroxyl, carbonyl, carboxyl and carboxylic functional group. The presence of adsorbed water is explicated by the peak seen at 3390 cm^{-1} and this is due to O–H stretching vibrations [40–42]. Stretching of the carbonyl and carboxyl groups are observed at 1720 and 1615 cm^{-1} . Vibrations from graphitic domain are well predominant by the peak seen at 1050 cm^{-1} . Presence of various functional groups in GO makes it to be in hydrophilic nature. But it is converted into hydrophobic in nature while reducing to graphene oxide.

The FTIR bands belonging to CN in the region between 2000 and 400 cm^{-1} in Fig. 4a demonstrate and establish the presence of both bending and stretching vibrations of NbO_6 octahedron. At 647 cm^{-1} we observe a broad envelope and this is designated to the mentioned stretching and bending modes of the NbO_6 octahedron [43].

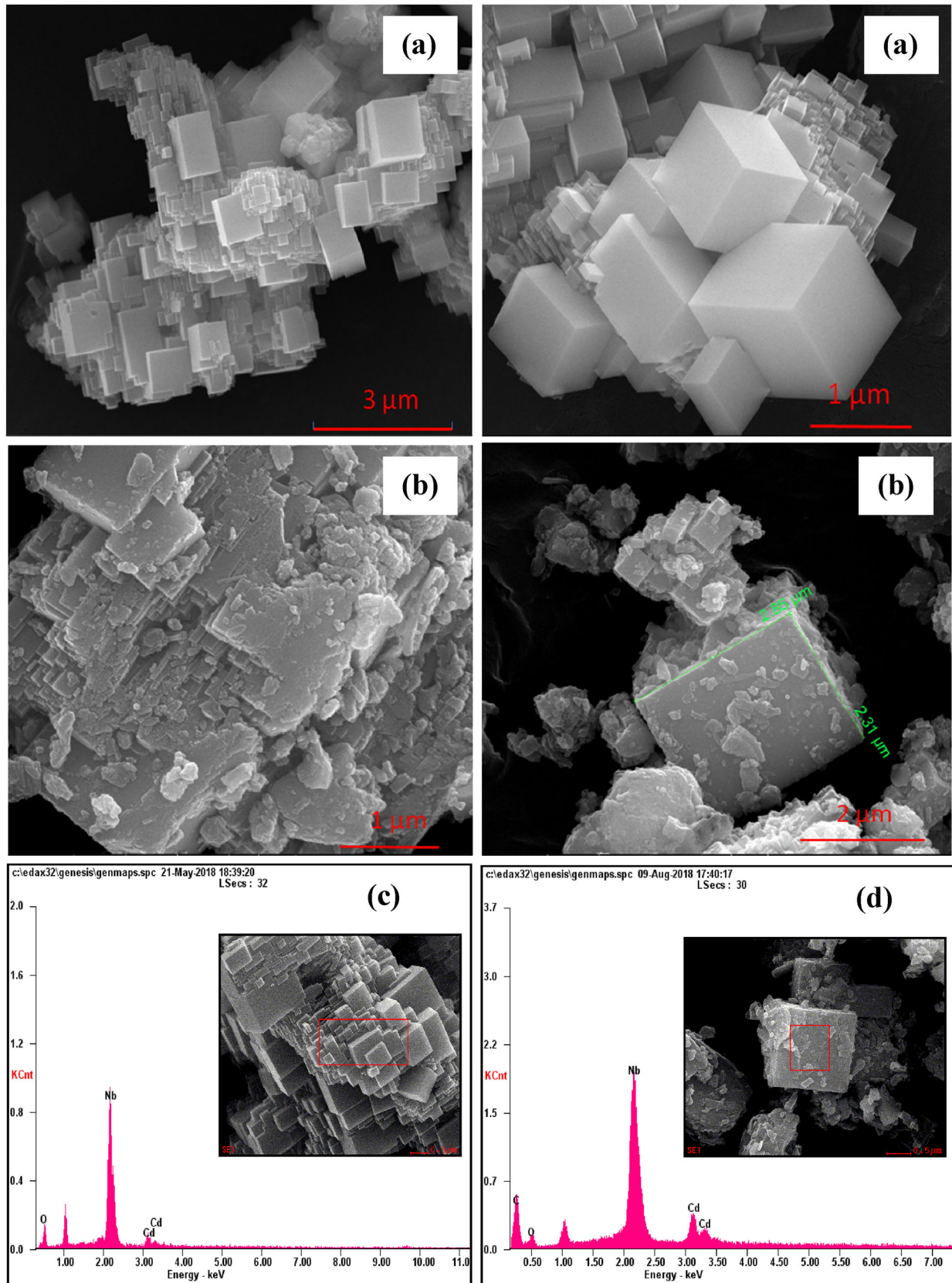


Fig. 2 **a** Morphology of CN and **b** morphology of RGO/CN, **c** compositional analysis of CN and **d** compositional analysis of RGO/CN

Table 1 Elemental composition of CN

ELEMENT	Wt%	At%
OK	30.85	72.68
NbL	58.61	23.78
CdL	10.54	3.54
Matrix	Correction	ZAF

Table 2 Elemental composition of RGO/CN

Element	Wt%	At%
CK	74.86	87.09
OK	12.56	10.97
NbL	07.46	01.12
CdL	05.12	00.82
Matrix	Correction	ZAF

Variations in intensity are noted corresponding to the peaks belonging to hydroxyl, carbonyl and carboxyl functional group in Fig. 4a, the spectra belonging to RGO/CN. Reduction of graphene oxide is dominantly shown by the peaks centred at 3457, 1632 and 1404 cm^{-1} . Distortion of Nb–O is revealed by the sharp stretching vibration seen at 637 cm^{-1} . This distortion also brings into light that graphene sheets are fastened within the columbite CN. The compiled vibrational assignments are shown in Table 3.

4.2 FT-Raman spectral analysis

Using Nd-YAG laser source coupled BRUKER RFS 27: stand-alone FT-Raman Spectrometer, the Raman spectra was analysed in a scan range of 4000–50 cm^{-1} . This analysis was done on GO, CN and RGO/CN to ascertain the extent of reduction of GO and structural changes supported with graphene in CN and is presented in Fig. 4b. In carbon-based materials, D bands are formed owing to the breathing mode of $K\alpha$ point photons belonging to A_{1g} symmetry. G bands are formed because of scattering of order one due to the photon belonging to atoms of carbon in E_{2g} mode of sp^2 hybridized state [44]. Raman spectra of GO nano sheets illustrated in Fig. 4b displays a peak at 1610 cm^{-1} indicating the strong D band and at 1295 cm^{-1} show the weak G band with calculated intensity ratio I_D/I_G as 0.8755. The observed low intensity ratio infers that exfoliated GO

consists of both sp^2 and sp^3 hybridized carbon content after oxidation.

In Fig. 4b, the Raman spectra of CN, the lowest frequency band at 77 cm^{-1} is due to the lattice vibrations. At 602 cm^{-1} and 241 cm^{-1} we observe sharp peak which indicate the vibrations due to stretching of terminal δ (O–Nb–O) in F_{2g} mode [45]. The vibrations noted from 700 to 500 cm^{-1} wavelength region is owing to the Nb–O bridge and those seen below 500 cm^{-1} is because of the Nb–O chain vibration. The stretching of Cd–O mostly occurs at lesser wavelength regions.

Figure 4b, the spectra of RGO/CN show a rise in the value of ratio of intensity of D and G band ($I_D/I_G = 1.079$) than that observed in GO. This indicates the reduction of graphene oxide. Also, the characteristic Raman band shift identified at 550, 638, 1296 and 1592 cm^{-1} indicate the availability of orthorhombic CN in the reduced graphene oxide layers [44].

4.3 Band gap determination

The dependence of absorbance with wavelength for CN and RGO/CN nanocomposite is shown in Fig. 5a and b. Absorption peak shown at about 253 nm in Fig. 5a relates to the optical absorption of CN. Further, the peak at 221 nm in Fig. 5b shows optical absorption in RGO/CN. The blue-shift in the optical spectra of RGO/CN when compared to CN is due to the bond among CN and RGO layers. Moreover, in RGO layers there is a wavelength shift in the absorption edge of nanocomposites based with graphene due to the Burstein-Moss effect [46]. This blue-shift in RGO/CN is due to the potential barriers formed by the limiting electron transfer exhibited among the levels of CN. This indicate that the energy necessary to excite and transfer RGO/CN increases.

Figure 5c and d shows the linear plot of $(\alpha h\nu)^2$ with energy of photon for CN and RGO/CN, respectively. The optical band gap corresponding to CN and RGO/CN obtained by extrapolating a straight line from the plot of $(\alpha h\nu)^2$ with energy of photon are 3.5107 eV and 4.024 eV, respectively. The raise in band gap energy of RGO/CN composite when compared to CN system is due to structural interaction of CN. The band gap of RGO/CN composite can also be regulated by the interaction of GO with CN.

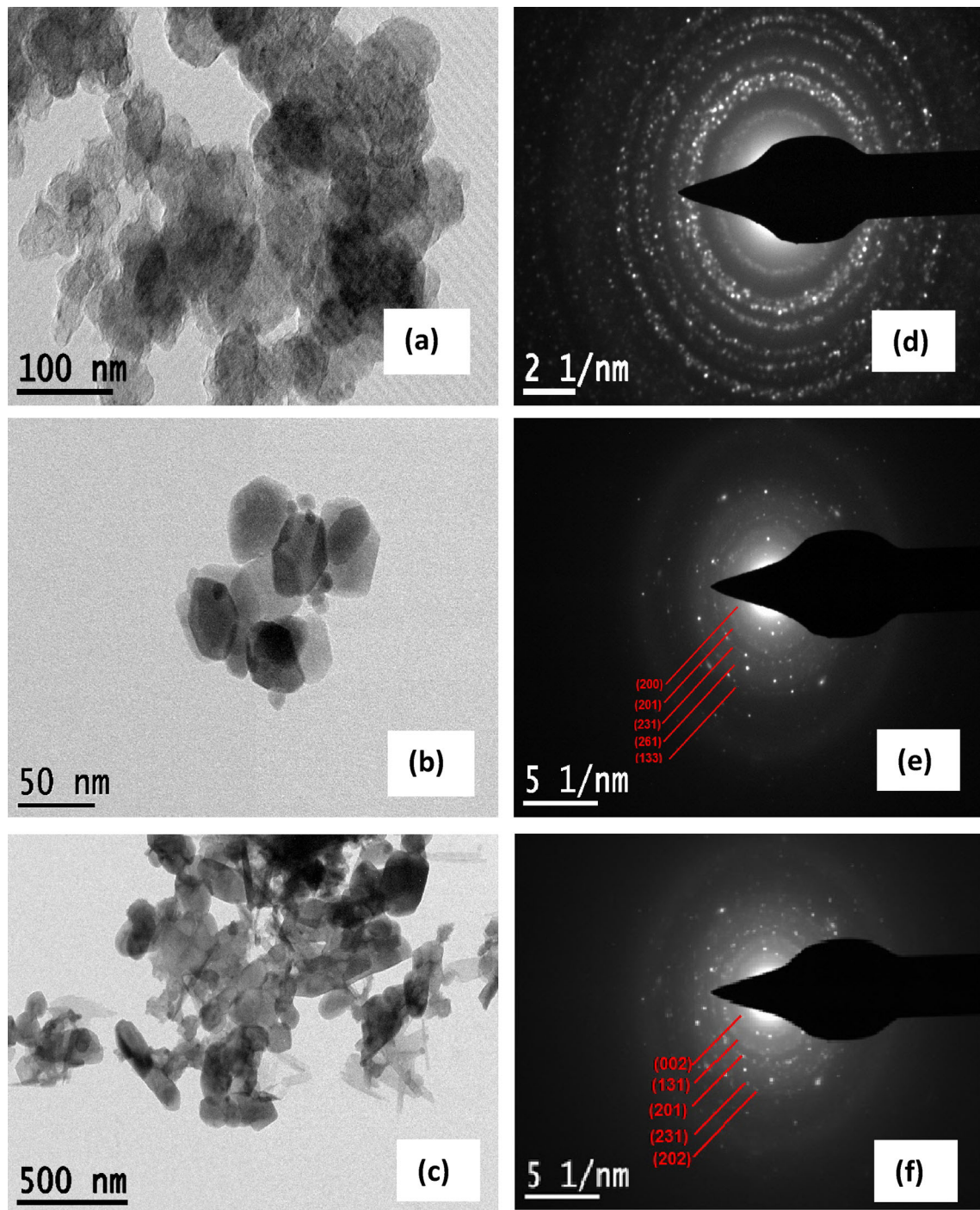


Fig. 3 HRTEM images of **a** GO, **b** CN and **c** RGO/CN, SAED pattern of **d** GO, **e** CN and **f** RGO/CN

5 Thermal studies of CN and RGO/CN

To evaluate the stability of synthesized CN and RGO/CN materials towards the change in temperature, a NETZSCH5 simultaneous thermogravimetric (TG) analyser was used by increasing the temperature of the samples at a rate of $10\text{ }^{\circ}\text{C min}^{-1}$ in

nitrogen atmosphere. The recorded curves are revealed in Fig. 6a and b. In the TG curve corresponding to CN presented in Fig. 6a, we see that when the temperature was raised beyond $363.4\text{ }^{\circ}\text{C}$ the mass remained the same till $1000\text{ }^{\circ}\text{C}$. However, there is a drastic loss of mass (28.2%) from 1000 to

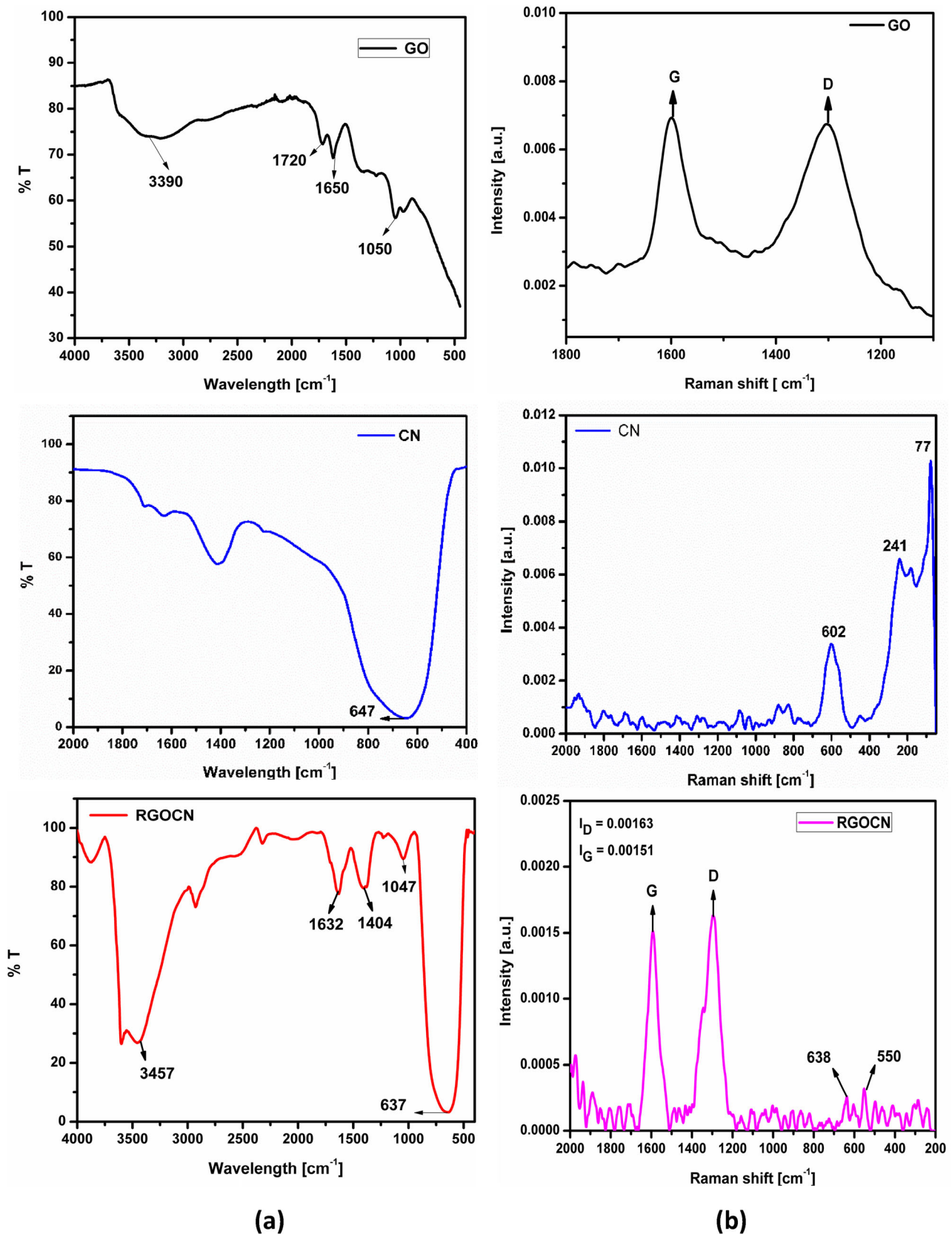


Fig. 4 a FT-IR spectra of GO, CN and RGO/CN, b FT-Raman spectra of GO, CN and RGO/CN

1150 °C. The DSC curve explicit a strong endothermic peak at 1135 °C indicating the decay of unreacted CdO content in the formed CN [45]. Further, the

prominent peak at 1345.9 °C indicates the melting point of CN.

The thermal behaviour of RGO/CN nanocomposite is seen in Fig. 6b. At 467.4 °C we see a strong exothermic peak with 17.63% weight loss that occurred during the oxidation of graphene [47]. Correspondingly in the TG–DSC curve of RGO/CN, the evaporation of CdO found in RGO/CN generate a strong endothermic peak at 1196.7 °C followed by a weight loss of 35.66%. Moreover, the temperature of melting occurred at 1399 °C. Thus, we note betterment in the thermal stability of RGO/CN.

Table 3 FTIR spectral assignments of GO, CN and RGO/CN

GO (cm ⁻¹)	CN (cm ⁻¹)	RGO/CN (cm ⁻¹)	Assignment
3390		3457	~ OH
1720, 1650		1632	~ C=O
		1404	~ C–O
1050		1047	~ C–O–C
	647	637	~ Nb–O

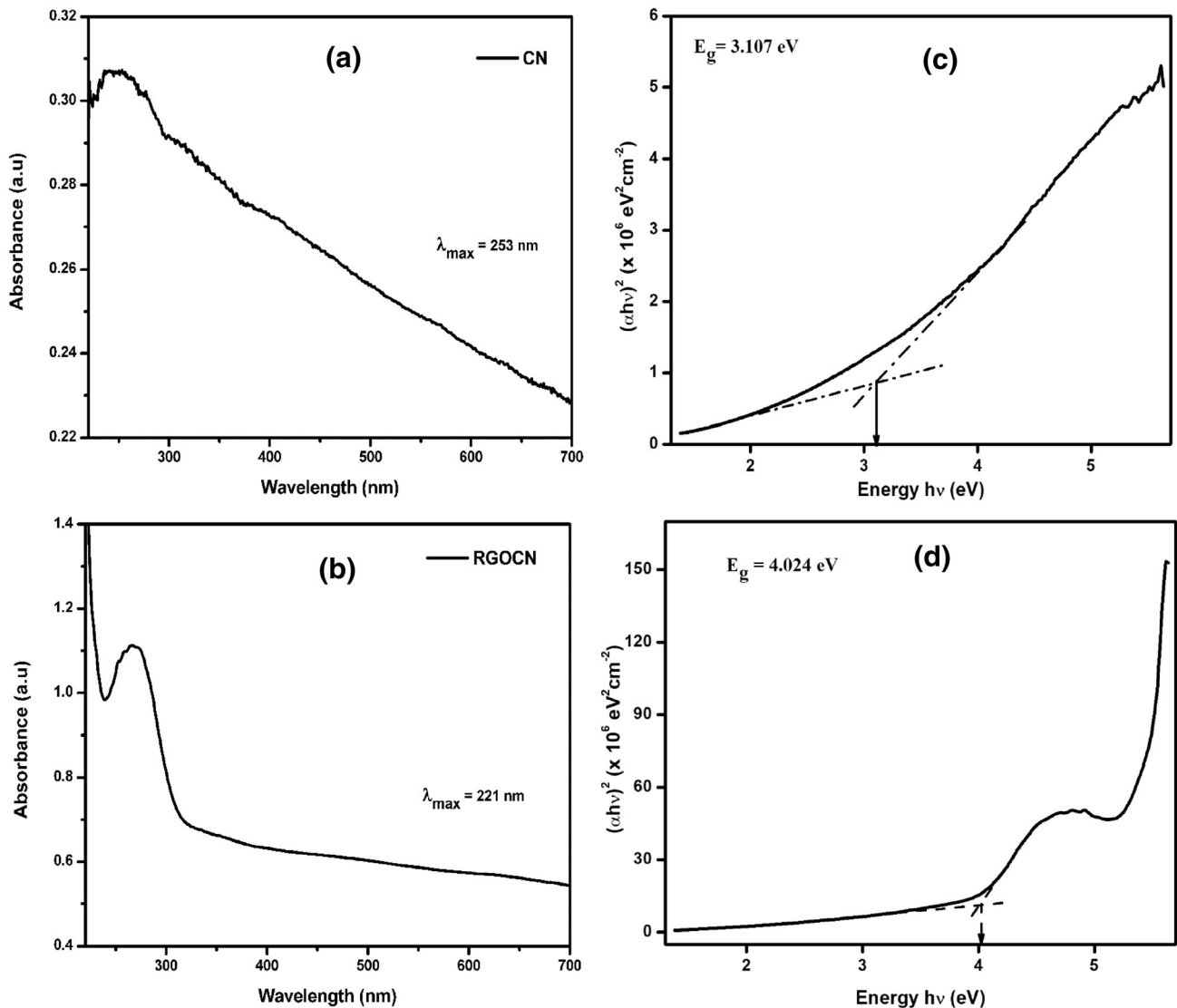


Fig. 5 **a** Plot of absorbance with wavelength for CN. **b** Plot of absorbance with wavelength for RGO/CN, **c** plot of $(\alpha hv)^2$ with $h\nu$ for CN, **d** plot of $(\alpha hv)^2$ with $h\nu$ for RGO/CN

6 Ferroelectric hysteresis studies

Polarization versus electric field (P–E loop) data were collected and analysed by a 609E–6 high voltage amplifier networked with 4 kV precision Radiant premier ferroelectric test system at 300 K. The P–E loop is a non-ideal curve generated due to the leakage current produced by oxygen vacancy [48]. The P–E loop in Fig. 7a and b illustrates the hysteresis behaviour of CN and RGO/CN samples for an applied electric field of 2.5 kV cm^{-1} and 4.5 kV cm^{-1} , respectively at ambient temperature.

The obtained P–E curve reveals promising ferroelectric nature in both CN and RGO/CN nanostructures. The spontaneous polarization (P_s) for CN nanostructure was found to be $0.0244 \text{ } \mu\text{C cm}^{-2}$ and its remanent polarization (P_r) and coercive electric field (E_c) were observed at $0.0151 \text{ } \mu\text{C cm}^{-2}$ and -1.30 kV cm^{-1} , respectively [49].

The observed coercive field (E_c) of -2.39 kV cm^{-1} at room temperature for RGO/CN shown in Fig. 7b shows an increase in value when compared with CN. The spontaneous polarization (P_s) and remanent polarization (P_r) for RGO/CN nanocomposite at a higher electric field of 4.5 kV was found to be $\sim 0.0685 \text{ } \mu\text{C cm}^{-2}$ and $0.0461 \text{ } \mu\text{C cm}^{-2}$, respectively. Thus, an enhancement in remanent polarization was observed in RGO/CN nanocomposite and this indicates its ferroelectric nature. Squareness of polarization (R_{sq}) of CN and RGO/CN was estimated as 0.684 and 0.797 respectively using the relation,

$$R_{sq} = \frac{P_r}{P_s} + \frac{P_{1.1E_c}}{P_s} \quad (1)$$

7 Electrochemical studies

7.1 Cyclic voltammetry

The electrochemical studies were done using biologic-240 electrochemical workstation. CN/RGO/CN slurry was prepared by continuously mixing the electrode material in *N*-methyl-2-pyrrolidone using carbon black and polyvinylpyrrolidone as binder [50] in the weight ratio of 70:20:10. This prepared slurry was layered as a thin coat in a carbon paper of size $1 \text{ cm} \times 1 \text{ cm}$. This working electrode was then dried at $80 \text{ }^\circ\text{C}$ for about 30 min and desiccated overnight. A three-electrode system was used to determine the

electrochemical properties of CN and RGO/CN samples. Throughout the entire electrochemical analysis, an electrode of saturated calomel acted as reference electrode and a platinum wire served as counter electrode. The potential window for scanning was set from -0.2 to $+1.0 \text{ V}$. Also, the electrodes were scanned for various scan rates in $0.1 \text{ M H}_2\text{SO}_4$ electrolyte. Throughout the analysis, the current was observed as a function of voltage (potentiostatic mode).

In the CV curves of CN presented in Fig. 8a we see that for an increase in scan rate, the dominant Faradaic process (both oxidation and reduction) leads to variation of redox peaks. Moreover, there is a gradual increase in the area of CV curves with increase in scan rate. This endorses the pseudo-capacitance process. Further, when the scan rate was increased an increase in redox current was identified. Several oxidation and reduction peaks are observed owing to the different faces of the major crystalline phase and their different reactivity. Moreover, these are likely to manifest as different potentials [51].

The electrochemical reaction at CN electrode is given by the following relation.



Figure 8b, the CV representation of RGO/CN indicates reversible electrochemical properties owing to the availability of RGO. In the potential ranging from 0.2 to 1 V , RGO/CN exhibit enhanced Faradaic behaviour than CN. We also observe a rise in the redox peak reflecting the inclusion of graphene and thereby the hybrid capacity of RGO/CN electrode is revealed. The interlinking of RGO and CN generates excellent charge transfer kinetics in RGO/CN.

The specific capacitance for CN and RGO/CN electrodes were estimated using [52] the relation

$$C_{sp} = \frac{\int IdV}{vmV}. \quad (3)$$

Here the response current is indicated by I , the potential window by V , the recorded scan rate by v and the active material mass on electrode by m . Table 4 presents the obtained results. While moving from higher to lower potential regions we see a continuous shift in the redox peak of both CN and RGO/CN. Also, an increase in the rate of scan generates an increase among redox peak in the potential separation. This can be owing to the influence of

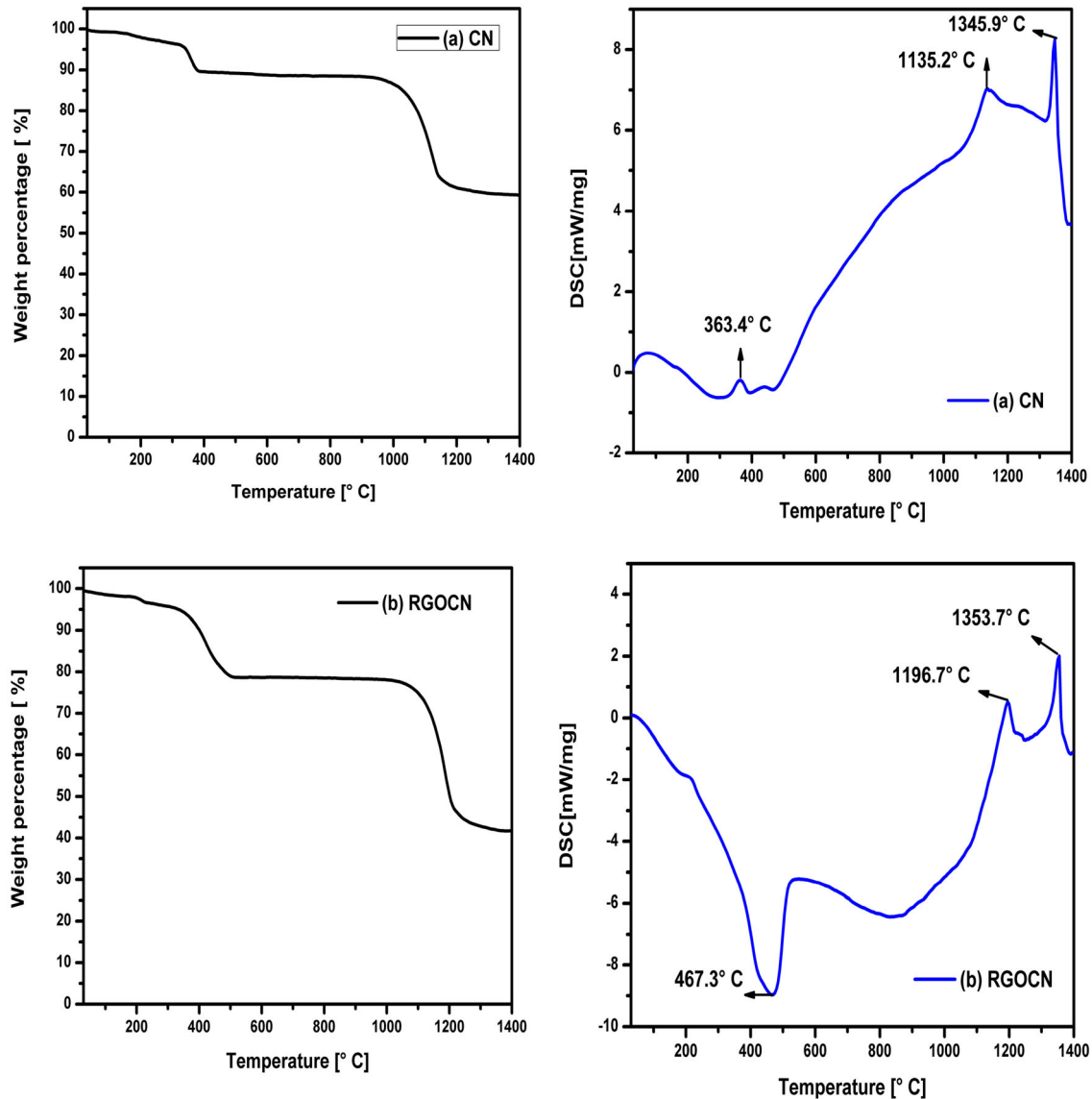


Fig. 6 **a** TG and DSC curve of CN, **b** TG and DSC curve of RGO/CN

ohmic resistance and polarization effect present in the material of the electrodes. Moreover, quasi-reversible nature of electrochemical reaction shows that the irreversibility degree turns to be large when the scan rates increase [52]. The loading of active material on the electrode contributes to the intrinsic activity of the electrode. When the loading increases on the electrode, the distance for the transport of electrons on the electrode increases and this supports a faster charge transfer on the electrode. Figure 8c and d displays the 3D-cyclic voltammetry (3D-CV) curves of the CN and RGO/CN electrode for various scan rates. There is a noticeable change in the CV curves for different scan rates. Also, information on the

charge storage mechanism of capacitors during various potential scan rates is clearly understood.

The impact of the scan rate on the specific capacitance of CN and RGO/CN presented in Fig. 8e shows a reduction in value of specific capacitance with scan rate. When there is a rise in scan rate owing to diffusion of H^+ ion into the electrode material intercalation/deintercalation of H^+ metal cations occurs. H^+ metal cations can easily intercalate inside RGO/CN hybrids electrode at lower scan rate. However, at higher scan rates RGO/CN hybrid electrodes shows a decrease in the capacitance. This decrease is because of the transfer rate of electrolytes which enabled depletion/saturation of ions in the electrolytes within

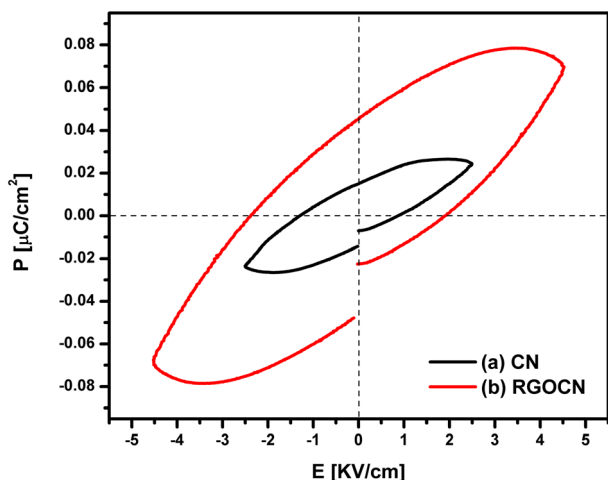


Fig. 7 P-E loop of **a** CN and **b** RGO/CN

the electrode during the redox process. When the ion transfer in the electrolyte turns faster, hydrogen ions inclusion onto the nanocomposites becomes easier [24]. Also, we see that presence of RGO in CN has raised its specific capacitance.

In the chosen potential window of -0.2 to 1.0 V with 10 mV s^{-1} scan rates, the cyclic stability of CN and RGO/CN were measured for 500 cycles and the output is presented in Fig. 8f. From the graph, we understand that, RGO/CN binary nanocomposites retain 92% of original value when 500 cycles were over and this is a greater value when compared with CN. The superior reversibility and cyclic stability possessed by the nanocomposite is thus revealed.

7.2 Galvanostatic charge–discharge (GCD) measurement

GCD studies were carried out with potential ranging between 0 and 1 V for various current densities. Figure 9a and b illustrates the charge-discharge functioning of CN and RGO/CN in 0.1 M H_2SO_4 aqueous electrolytic medium. From the charge-discharge pattern, the reversible behaviour of CN and RGO/CN with the discharge time is identified. However, deviations are observed for CN and RGO/CN due to electrochemical decomposition in electrode preparation. This is due to limitation of electrode material's stability. Therefore, only a minimum part of electrical double layer was involved during discharging in RGO/CN.

The estimated specific capacitance of CN and RGO/CN is tabulated in Table 5. It is observed that

graphene when attached with cube-like CN enhances the storage ability of RGO/CN. The table also record the GCD behaviour of CN and RGO/CN for various values of current density in H_2SO_4 electrolytic medium. A maximum value of 7.97 F g^{-1} and 58.2 F g^{-1} specific capacitance was seen in CN and RGO/CN for the low concentration aqueous electrolytic medium of 0.1 M H_2SO_4 when the current density was 1 A g^{-1} . We see an increase in specific capacitance of RGO/CN due to the reduction of GO with CN. The results observed in GCD modes agree well with those attained in the cyclic voltammetry experiments.

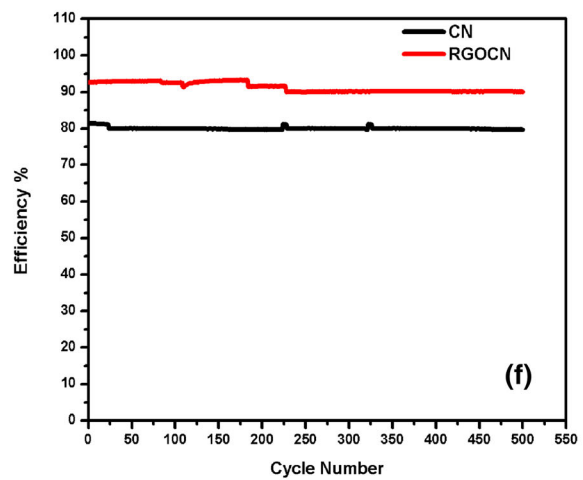
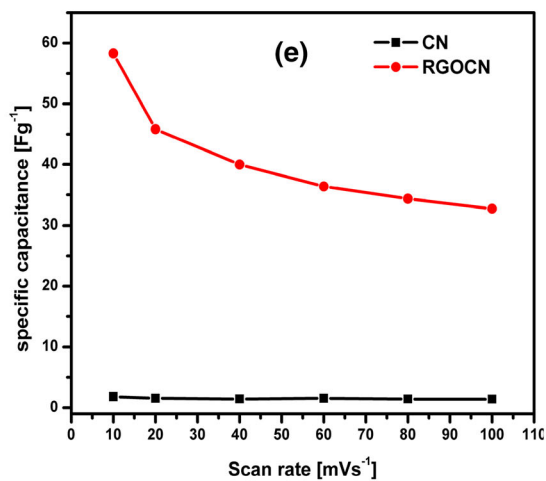
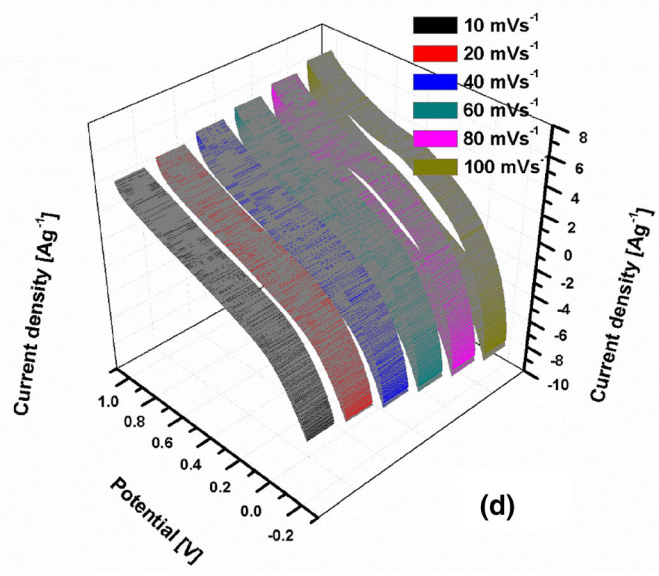
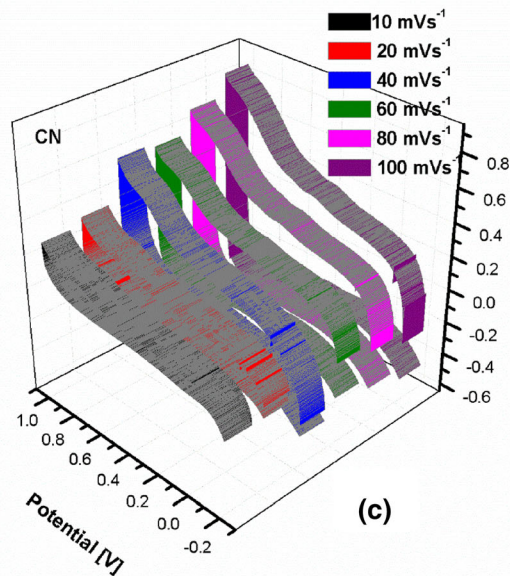
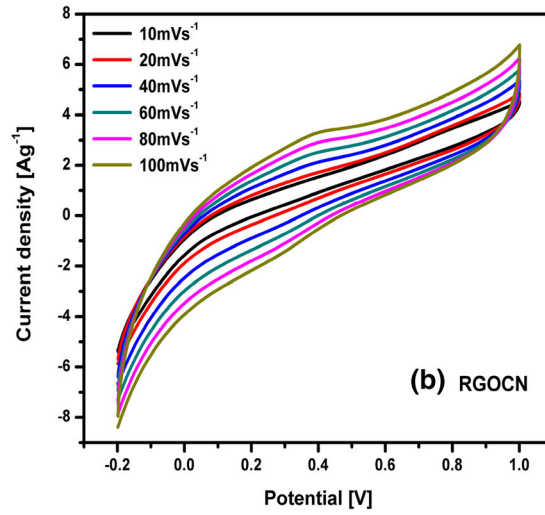
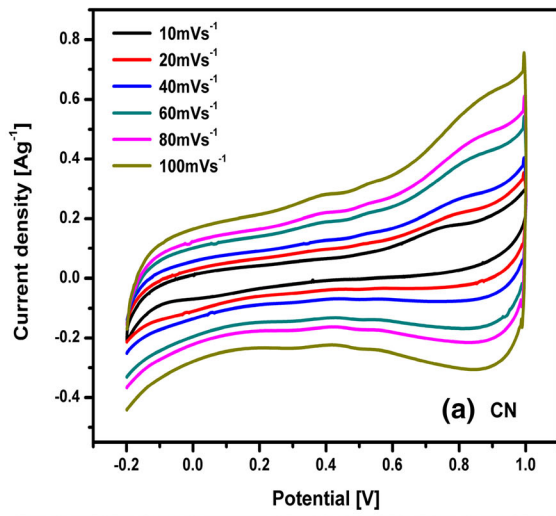
Variation in specific capacitance CN and RGO/CN for different current densities represented in Fig. 9c also shows lowering in the value of specific capacitance value in the CN and RGO/CN electrodes when the value of current density rise. This decrease in specific capacitance resulted due to the internal resistance exhibited by them [53, 54]. At higher current density, only the material which was available in the outer layer of the electrode was used effectively and thereby resulted in lower value of capacitance.

The energy density and power density of both CN and RGO/CN electrodes were calculated using the following equations.

$$\text{Energy density } (E_s) = \frac{1}{2} \left(\frac{C_s \times dV^2}{3.6} \right) \quad (4)$$

$$\text{Power density } (P) = \left(\frac{3600 \times E_s}{dt} \right), \quad (5)$$

where the potential windows is indicated by dV , specific capacitance is represented by C_s , power density by P and the discharge time by dt . For CN electrode, a maximum energy density of 1.1 Wh kg^{-1} with consuming power density of 415 W kg^{-1} was noted at 1 A g^{-1} . Also, the maximum energy density obtained for RGO/CN electrode was 8.08 Wh kg^{-1} and its consuming power density was 4137 W kg^{-1} at 1 A g^{-1} . Table 6 clearly shows that moderate energy density and high-power density of RGO/CN brings about acceptable magnitudes for energy storage behaviour when compared with few reported materials [55]. It is further reflected from Table 7 that RGO/CN stay as a good material for fabricating supercapacitor since enhancement in specific capacitance of RGO/CN composite material is observed. Obtained results are permissible for producing energy storage devices when compared with other reported graphene composites for low electrolytic



◀**Fig. 8** **a** Cyclic voltammetry curve in 0.1 M H₂SO₄ for CN, **b** cyclic voltammetry curve in 0.1 M H₂SO₄ for RGO/CN, **c** 3D-cyclic voltammetry curves of CN and **d** 3D-cyclic voltammetry curves of RGO/CN, **e** variation of specific capacitance as a function of scan rate for CN and RGO/CN and **f** performance comparison of CN and RGO/CN electrode for 500 cycles

concentration even though prominent preparation methods were used.

The cyclic stability of CN and RGO/CN were measured in 0.1 M H₂SO₄ using GCD technique for 500 cycles at 2 A g⁻¹ and the output is explored from Fig. 10a, b and c. From the graph, it is understood that, RGO/CN binary nanocomposites retain 98% of original value when 500 cycles were over and this is enhanced when compared with CN.

7.3 Electrochemical impedance spectroscopy (EIS)

The transfer of charge and its mechanism can be well understood by the EIS method in a solid-state device. The synthesized CN and RGO/CN materials were coated on carbon paper and EIS measurements were obtained for a frequency range of 100 Hz to 7 MHz at 10 mV AC sine amplitude. Figure 11a and b represents the typical Nyquist impedance plots of CN and RGO/CN at room temperature. The electronic and ionic involvement can be described from the resistance offered by electrochemical cell. The ionic part is further explored to the separator resistance by means of the ions diffusion through the pores of the electrodes. The electronic resistance is calculated from the bulk resistivity of the electrode material, which includes contact resistance between current collecting substrate and the electrode making materials. The

intercept of real part (Z) reveals the ionic resistance of electrolyte at higher range of frequency. It further helps to estimate that the ionic resistance of electrolyte and is almost same for both impedance spectra. Also, Nyquist plots of CN and RGO/CN composite hybrid electrodes show a semicircular part with an inclined line. It is clearly identified that the large semicircle for the electrode is due to the high interfacial charge transfer resistance, which resulted from the low electrical conductivity of active substances. In the Nyquist plots, charge transfer resistance (R_2) is identified as a semicircle at high frequency region and fast diffusion of ions in the electrode materials as inclined line at low frequencies [58].

Further, the equivalent circuit was generated with Z fit analysis utilizing the EC lab software already programmed within the instrument and is displayed as inset in Fig. 11a and b. Equivalent circuit of both CN and RGO/CN consists of solution resistance (R_1), charge transfer resistance (R_2), double layer capacitance (C_2) and Warburg element (W). At higher frequency, the Nyquist plot of both electrodes appears as a semicircle and in the lower frequency range it is seen as a straight line.

The data obtained for CN electrode is fitted with one simple parallel R_2C_2 circuit connected in series with a resistor (R_1) and Warburg element (W_3) connected in series as depicted in Fig. 11a. The C_2 element for CN system is computed as 2.1 F g⁻¹. The resistance R_1 in CN equivalent circuit is due to ionic resistance of electrolyte and R_2 is related with the charge transfer resistance observed in the interface of electrode–electrolyte. W_2 represents Warburg resistance associated with linear part of low frequency.

Table 4 Specific capacitance of CN and RGO/CN at different scan rates

Scan rate (mV s ⁻¹)	Specific capacitance (F g ⁻¹) CN	Specific capacitance (F g ⁻¹) RGO/CN
10	1.83	58.33
20	1.58	45.83
40	1.45	40.00
60	1.58	36.38
80	1.43	34.37
100	1.41	32.75

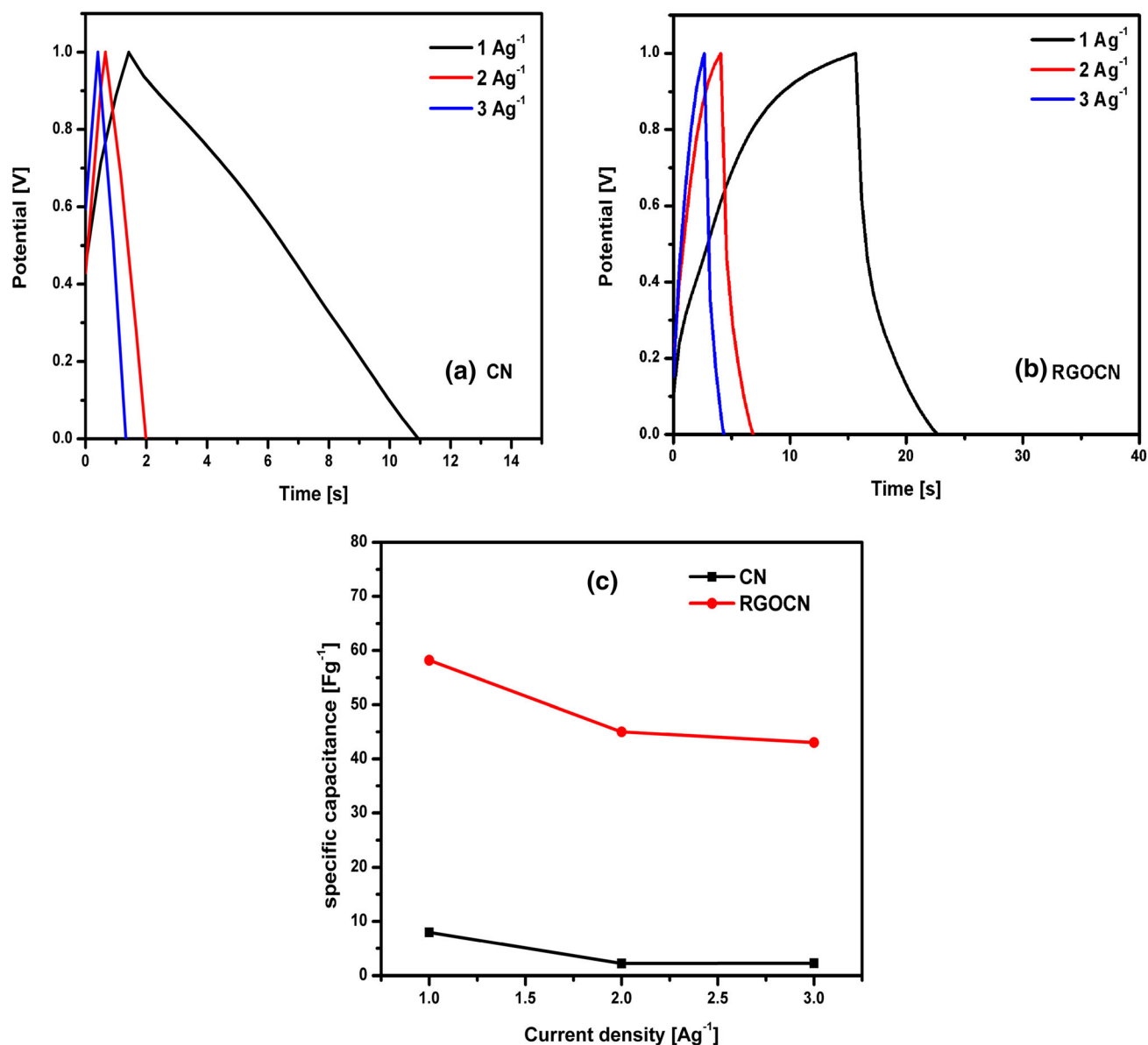


Fig. 9 **a** GCD charging/discharging profile of CN electrode, **b** GCD charging/discharging profile of RGO/CN electrode, and **c** variation of specific capacitance with current density for CN and RGO/CN

Table 5 Specific capacitance of CN and RGO/CN by GCD mode

Current density (A g ⁻¹)	Specific capacitance (F g ⁻¹)	
	CN	RGO/CN
1	7.97	58.2
2	2.18	45
3	2.22	43

For RGO/CN electrode, the observed C_2 element value of 65.2 F g^{-1} reveals one simple series R_2W_2 circuit connected in parallel with a capacitor C_1 and in series with solution resistance R_1 and is presented in Fig. 11b. RGO, when incorporated with CN alters its dielectric behaviour and this improves the electric conduction. At low frequency region, the Warburg element of CN shows pseudo-capacitance behaviour.

Table 6 Comparison of energy density of RGO/CN with other supercapacitor materials

Material	References	Energy density (Wh kg ⁻¹)	Power density (kW kg ⁻¹)
MnMoO ₄ on Ni foam	Mu et al. [42]	31.6	0.935
NiO/porous carbon	Wang et al. [42]	11.6	0.028
NiCo ₂ O ₄ /AC	Ding et al. [42]	6.8	2.8
NiCo ₂ O ₄ -MnO ₂ //AG	Kuang et al. [42]	5.8	2.5
RGO/CN	Present work	8.08	4.13

Table 7 Comparison chart of specific capacitance value of RGO/CN composite material with previous reported articles

Electrode material	Electrolyte	Preparation method	Specific capacitance C _s (F g ⁻¹)	References
CNT-graphene films	0.1 M H ₂ SO ₄	Drop casting, vacuum filtration, air brush spraying	14	[55]
Graphene/PANI hybrid paper	0.1 M H ₂ SO ₄	Vacuum filtration and polymerization	48.9	[55]
Functionalized graphene hydrogel	0.1 M H ₂ SO ₄	Hydrothermal method	23.9	[55]
Cobalt oxide-intercalated (GWCI)	0.5 M BMIM-BF ₄ /CH ₃ CN	Microwave irradiation	712	[56]
Graphene/MnO ₂	1 M Na ₂ SO ₄ aqueous electrolyte	Hydrothermal	192.2	[57]
Voids induced and graphene-wrapped nickel oxide (VGWN)	5 M KOH	Microwave irradiation	549	[18]
RGO/CN	0.1 M H ₂ SO ₄	Hydrothermal	58.2	Present work

The observed change in RGO/CN equivalent circuit in the low frequency region reflects the addition of RGO on CN [59]. Table 8 summarizes the values exhibited by the various circuit parameters for both CN and RGO/CN.

Comparing both electrodes, the RGO/CN hybrid electrode explores low R_2 value of 4.55 Ω and has a less inclined line, thereby showing an enhanced capacitive performance than that of the CN electrode (24.6 Ω). Those observed results may be due to the reversible redox reactions entangled with CN nanomaterials along with the better electrical conductivity of RGO/CN.

8 Conclusions

The orthorhombic structure exhibited by CN nanocomposite and the inclusion of RGO in CN were confirmed from the PXRD pattern. Hydrothermally prepared RGO/CN composite exhibited exfoliation of graphene sheets with mixed morphology of cubes and rectangular slab were revealed by HRSEM and

HRTEM analysis. The presence of different functional groups belonging to GO, CN and RGO/CN were understood through the FTIR and FT-Raman analysis. The optical band gap corresponding to CN and RGO/CN were found to be 3.5107 eV and 4.024 eV. Moreover, RGO/CN was identified with enhancement in remanent polarization, coercive electric field when compared with CN.

Electrochemical studies of CN and RGO/CN in low concentration 0.1 M H₂SO₄ electrolyte showed that RGO/CN display high surface area and enhanced specific capacitance for different scan rates than CN. Specific capacitance of RGO/CN was computed as 58.2 F g⁻¹ at 1 A g⁻¹. Maximum energy density of 8.08 Wh kg⁻¹ was obtained for RGO/CN electrode and its consuming power density was estimated to be as 4137 W kg⁻¹ at 1 A g⁻¹. Furthermore, RGO/CN electrode furnishes cyclic stability with 98% of capacitive retention after 500 cycles at 2 A g⁻¹ by GCD method. Magnitude of energy density and power density for RGO/CN showed the better performance of energy storage capacity than other few

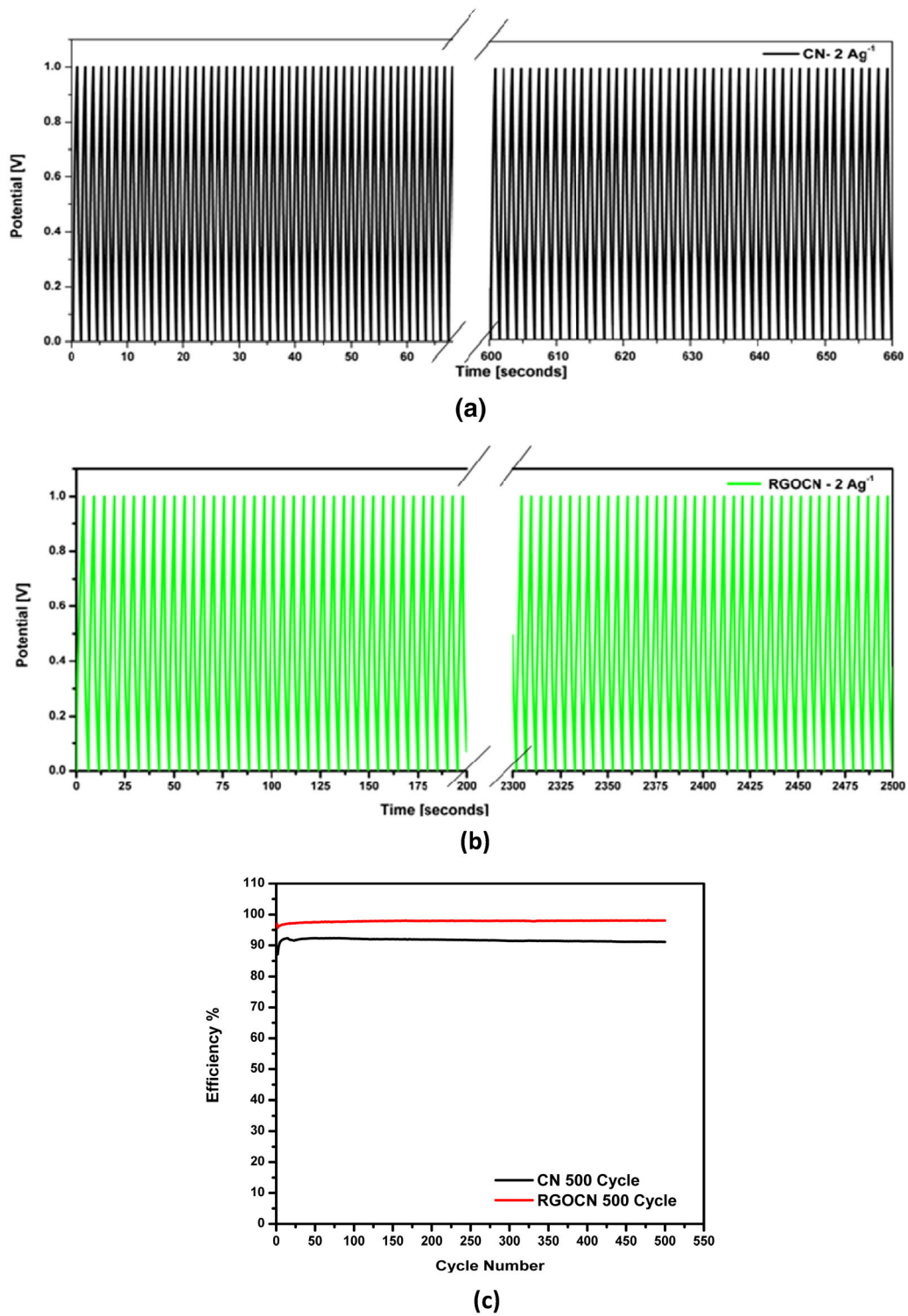


Fig. 10 **a** Cyclic stability of CN using GCD technique for 500 cycles. **b** Cyclic stability of RGO/CN using GCD technique for 500 cycles and **c** variation of specific capacitance with current density for 500 cycles—CN and RGO/CN

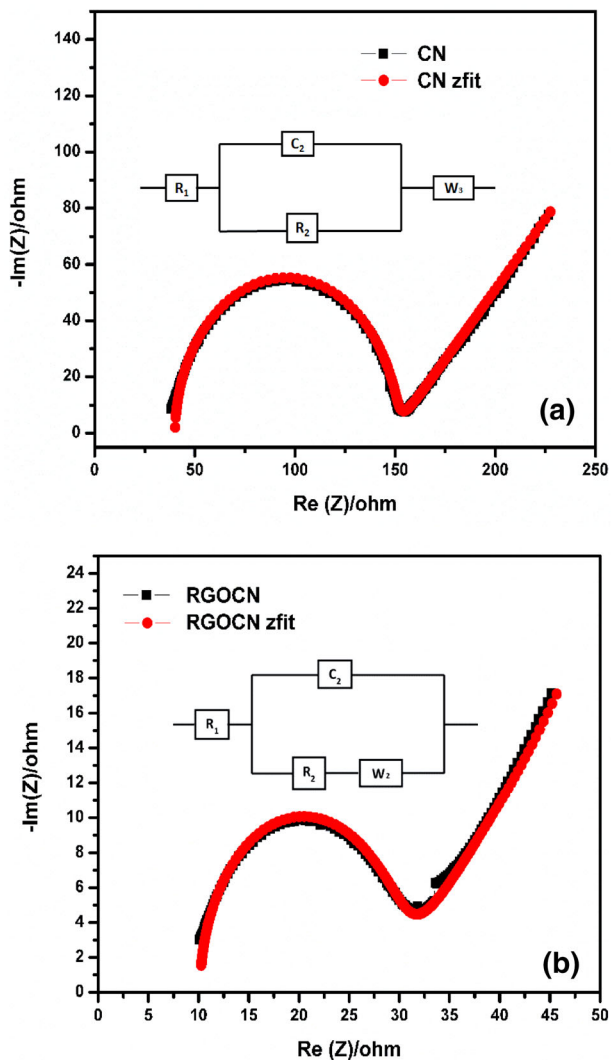


Fig. 11 Nyquist plots and normalized Z fit equivalent circuit for **a** CN and **b** RGO CN

Table 8 Circuit elements of CN and RGO CN

Circuit parameters	CN values	RGO CN values
R_1	0.3727 Ω	0.1848 Ω
C_2	2.1 $F g^{-1}$	65.2 $F g^{-1}$
R_2	24.61 Ω	4.548 Ω
Warburg element	185.9 $\Omega s^{-1/2}$	38.23 $\Omega s^{-1/2}$

reported materials. Thus, the obtained results well demonstrate the hybrid capacitive behaviour of both CN and RGO CN making it material of great interest for super capacitor applications.

Declarations

Conflict of interest The authors declare that they have no known competing financial interests or personal relationships that could have appeared to influence the work reported in this paper.

References

1. F.Z. Amir, V.H. Pham, E.M. Schultheis, J.H. Dickerson, Flexible, all-solid-state, high-cell potential supercapacitors based on holey reduced graphene oxide/manganese dioxide nanosheets. *Electrochim. Acta* **260**, 944–951 (2018)
2. C. Ogata, R. Kurogi, K. Awaya, K. Hatakeyama, T. Taniguchi, M. Koinuma, Y. Matsumoto, All-graphene oxide flexible solid-state supercapacitors with enhanced electrochemical performance. *ACS Appl. Mater. Interfaces* **9**(31), 26151–26160 (2017)
3. A.K. Geim, K.S. Novoselov, The rise of graphene. *Nat. Mater.* **6**, 183–191 (2007)
4. A. Garcia, A.F.B. Lopera, N. Ornelas-Soto, A.M. Garay-Tapia, F.R. Pérez, Á. Salazar, A general strategy for direct synthesis of reduced graphene oxide by chemical exfoliation of graphite. *Mater. Chem. Phys.* **218**, 51–61 (2018)
5. M. Batzill, The surface science of graphene: metal interfaces, CVD synthesis, nanoribbons, chemical modifications and defects. *Surf. Sci. Rep.* **67**, 83–115 (2012)
6. D.R. Dreyer, The chemistry of graphene oxide, in *Graphene Oxide: Reduction Recipes, Spectroscopy and Applications* (Springer, Cham, 2015), pp. 61–95
7. I.S. El-Hallag, M.N. El-Nahass, S.M. Youssry, R. Kumar, M.M. Abdel-Galeil, A. Matsuda, Facile in-situ simultaneous electrochemical reduction and deposition of reduced graphene oxide embedded palladium nanoparticles as high performance electrode materials for supercapacitor with excellent rate capability. *Electrochim. Acta* **314**, 124–134 (2019)
8. R. Kumar, S. Sahoo, E. Joanni, R.K. Singh, K. Maegawa, W.K. Tan, G. Kawamura, K.K. Kar, A. Matsuda, Heteroatom doped graphene engineering for energy storage and conversion. *Mater. Today* **39**, 47–65 (2020)
9. R. Kumar, S. Sahoo, E. Joanni, R.K. Singh, W.K. Tan, K.K. Kar, A. Matsuda, Recent progress in the synthesis of graphene and derived materials for next generation electrodes of high performance lithium ion batteries. *Prog. Energy Combust. Sci.* **75**, 100786 (2019)
10. R. Kumar, S. Sahoo, E. Joanni, R.K. Singh, R.M. Yadav, R.K. Verma, D.P. Singh, W.K. Tan, A. Pérez, S.A. del Pino, A. Moshkalev, Matsuda, A review on synthesis of graphene,

- h-BN and MoS₂ for energy storage applications: Recent progress and perspectives. *Nano Res.* **12**, 2655–2694 (2019)
11. F. Li, X. Jiang, J. Zhao, S. Zhang, Graphene oxide: a promising nanomaterial for energy and environmental applications. *Nanomater. Energy* **16**, 488–515 (2015)
 12. W. Deng, X. Ji, M. Gomez-Mingot, F. Lu, Q. Chen, C.E. Banks, *Chem. Commun.* **48**, 2770 (2012)
 13. E. Mitchell, J. Candler, F. De Souza, R.K. Gupta, B.K. Gupta, L.F. Dong, High performance supercapacitor based on multilayer of polyaniline and graphene oxide. *Synth. Met.* **199**, 214–218 (2015)
 14. R. Imran Jafri, N. Rajalakshmi, S. Ramaprabhu, Nitrogen doped graphene nano platelets as catalyst support for oxygen reduction reaction in proton exchange membrane fuel cell. *J. Mater. Chem.* **20**, 7114–7117 (2010),)
 15. V. Dhand, K.Y. Rhee, H.J. Kim, D.H. Jung, A comprehensive review of graphene nanocomposites: research status and trends *J. Nanomater.*, Article ID 763953 (2013)
 16. R. Kumar, S. Youssry, K.Z. Ya, W.K. Tan, G. Kawamura, A. Matsuda, Microwave-assisted synthesis of Mn₃O₄-Fe₂O₃/Fe₃O₄@rGO ternary hybrids and electrochemical performance for supercapacitor electrode. *Diam. Relat. Mater.* **101**, 107622 (2019)
 17. R. Kumar, R.K. Singh, A.R. Vaz, R. Savu, S.A. Moshkalev, Self-assembled and one-step synthesis of interconnected 3D network of Fe₃O₄/reduced graphene oxide nanosheets hybrid for high-performance supercapacitor electrode. *ACS Appl. Mater. Interfaces* **9**(10), 8880–8890 (2017)
 18. R. Kumar, R.K. Singh, R. Savu, P.K. Dubey, P. Kumar, S.A. Moshkalev, Microwave- assisted synthesis of void-induced graphene-wrapped nickel oxide hybrids for supercapacitor applications. *RSC Adv.* **6**, 26612–26620 (2016)
 19. X. Chen, H. Fan, Y. Fu, L. Liu, J. Chen, Low-temperature fabrication and crystallization behavior of Pb(Mg_{1/3}Nb_{2/3}O₃) crystallites by a hydrothermal process. *J. Alloys Compd.* **469**(1-2), 322–326 (2009)
 20. M. Rahimi-Nasrabadi, V. Pourmohamadian, M.S. Karimi, H.R. Naderi, M.A. Karimi, K. Didehban, M.R. Ganjali, Assessment of supercapacitive performance of europium tungstate nanoparticles prepared via hydrothermal method. *J Mater. Sci. Mater Electron.* **28**, 12391–12398 (2017)
 21. H.R. Naderi, A. Sobhani-Nasab, M. Rahimi-Nasrabadi, M.R. Ganjali, Decoration of nitrogen-doped reduced graphene oxide with cobalt tungstate nanoparticles for use in high-performance supercapacitors. *Appl. Surf. Sci.* **423**, 1025–1034 (2017)
 22. A. Sobhani-Nasab, M. Rahimi-Nasrabadi, H.R. Naderi, V. Pourmohamadian, F. Ahmadi, M.R. Ganjali, H. Ehrlich, Sonochemical synthesis of terbium tungstate for developing high power supercapacitors with enhanced energy densities. *Ultrason. Sonochem.* **45**, 189–196 (2018)
 23. J. Li, M. Ostling, Prevention of graphene restacking for performance boost of supercapacitors—a review. *Crystals* **3**, 163 (2013)
 24. U. Patil, S.C. Lee, S. Kulkarni, J.S. Sohn, M.S. Nam, S. Han, S.C. Jun, Nanostructured pseudocapacitive materials decorated 3D graphene foam electrodes for next generation supercapacitors. *Nanoscale* **7**, 6999 (2015)
 25. C. An, K. Tang, C. Wang, G. Shen, Y. Jin, Y. Qian, Characterization of LiNbO₃ nanocrystals prepared via a convenient hydrothermal route. *Mater. Res. Bull.* **37**, 1791–1796 (2002)
 26. A.Z. Simões, A.H.M. González, A. Ries, M.A. Zaghete, B.D. tojanovic, J.A. Varela, Influence of thickness on crystallization and properties of LiNbO₃ thin films. *Mater. Charact.* **50**, 239–244 (2003)
 27. M. Liu, D. Xue, An efficient approach for the direct synthesis of lithium niobate powders. *Solid State Ionics* **177**, 275–280 (2006)
 28. J. Liu, I. Shakir, D.J. Kang, Lithium niobate nanoflakes as electrodes for highly stable electrochemical supercapacitor devices. *Mater. Lett.* **119**, 84–87 (2014)
 29. C. Daniela, D.V. Marcano, J.M. Kosynkin, A. Berlin, Z. Sinitskii, S.A. Slesarev, L.B. Alemany, W. Lu, J.M. Tour, Improved synthesis of graphene oxide. *ACS Nano* **4**(8), 4806–4814 (2010)
 30. M.I.S. Kumar, S. Shahil Kirupavathy, E. Jerusha, S. Sureshkumar, M. Vinolia, Synthesis and characterization of novel reduced graphene oxide supported barium niobate (RGOBN) nanocomposite with enhanced ferroelectric properties and thermal stability. *J. Mater. Sci. Mater. Electron.* **29**, 19228–19237 (2018)
 31. X. Jiao, Y. Qiu, L. Zhang, X. Zhang, Comparison of the characteristic properties of reduced graphene oxides synthesized from natural graphites with different graphitization degrees. *RSC Adv.* **7**(82), 52337–52344 (2017)
 32. R.F. Samigullina, T.I. Krasnenko, M.V. Rotermel, A.P. Tyutyunnik, S.G. Titova, O.M. Fedorova, Crystal-chemical and physicochemical properties of complex cadmium oxides with pyrochlore and columbite type of structure. *Mater. Chem. Phys.* **168**, 122–126 (2015)
 33. S.H. Huh, in *Thermal Reduction of Graphene Oxide, Physics and Applications of Graphene—Experiments*, ed. by S. Mikhailov (InTechOpen, London, 2011). ISBN: 978-953-307-217-3
 34. K. Venkateswarlu, M. Sandhyarani, T.A. Nellaippan, N. Rameshbabu, Estimation of crystallite size, lattice strain and dislocation density of nanocrystalline carbonate substituted

- hydroxyapatite by X-ray peak variance analysis. *Procedia Mater. Sci.* **5**, 212–221 (2014)
35. B. Fultz, J.M. Howe 2002, High-resolution TEM imaging, in *Transmission Electron Microscopy and Diffractometry of Materials* (Springer, Berlin). https://doi.org/10.1007/978-3-662-04901-3_10
 36. X. Gou, B. Wang, H. Liu, J. Yao, G. Wang, J. Yang, J. Park, Facile synthesis and characterization of graphene nanosheets. *J. Phys. Chem. C* **112**, 8192–8195 (2008)
 37. Y.-W. Hsu, T.-K. Hsu, C.-L. Sun, Y.-T. Nien, N.-W. Pu, M.-D. Ger, Synthesis of CuO/graphene nanocomposites for nonenzymatic electrochemical glucose biosensor applications. *Electrochim. Acta* **82**, 152–157 (2012)
 38. D. Das, A.K. Ganguli, Design of nanostructured cadmium tantalate and niobate and their photocatalytic properties. *RSC Adv.* **3**, 21697–21705 (2013)
 39. J. Sengupta, K. Das, U.N. Nandi, C. Jacob, Substrate free synthesis of graphene nanoflakes by atmospheric pressure chemical vapour deposition using Ni powder as a catalyst. *Bull. Mater. Sci.* **42**(4), 136 (2019)
 40. S. Ratha, C.S. Rout, Supercapacitor electrodes based on layered tungsten disulfide-reduced graphene oxide hybrids synthesized by a facile hydrothermal method. *ACS Appl. Mater. Interfaces* **5**, 11427–11433 (2013)
 41. T. Jiao, Y. Liu, Y. Wu, Q. Zhang, X. Yan, F. Gao, A.J.P. Bauer, J. Liu, T. Zeng, B. Li, Facile and scalable preparation of graphene oxide-based magnetic hybrids for fast and highly efficient removal of organic dyes. *Sci. Rep.* **5**, 12451 (2015)
 42. K. Krishnamoorthy, R. Mohan, S.-J. Kim, Graphene oxide as a photocatalytic material. *Appl. Phys. Lett.* **98**, 244101–244103 (2011)
 43. L.A. Bugaev, V.A. Shuvaeva, I.B. Alekseenko, K.N. Zhuchkov, R.V. Vedrinskii, Determination of the local structure of NbO₆ octahedra in the orthorhombic phase of a KNbO₃ crystal using EXAFS. *Phys. Solid State* **40**(6), 1001–1005 (1998)
 44. C. Balamurugan, S. Arunkumar, D.-W. Lee, Hierarchical 3D nanostructure of GdInO₃ and reduced graphene-decorated GdInO₃ nanocomposite for CO sensing applications. *Sensors Actuators Chem.* **234**, 155–166 (2016)
 45. R.F. Samigullina, M.V. Rotermel, I.V. Nikolaenko, T.I. Krasnenko, Phase Equilibria in the Nb₂O₅–CdO System and the Thermal Stability of Cd₂Nb₂O₇ and CdNb₂O₆. *Russ. J. Inorg. Chem.* **61**(2), 156–160 (2016)
 46. F. Soofivand, M. Salavati-Niasari, Co₃O₄/Graphene nanocomposite: pre-graphenization synthesis and photocatalytic investigation of various magnetic nanostructures. *RSC Adv.* **5**, 64346–64353 (2015)
 47. J. Wu, X. Shen, L. Jiang, K. Wang, K. Chen, Solvothermal synthesis and characterization of sandwich-like graphene/ZnO Nanocomposites. *Appl. Surf. Sci.* **256**, 2826–2830 (2010)
 48. C.A. Díaz-Moreno, J.A. López, Y. Ding, A.H. Macias, C. Li, R. B. Wicker, Multiferroic and optical properties of La_{0.05}Li_{0.85}NbO₃ and LiNbO₃ nanocrystals. *J. Nanotechnol.* **2018**(2), 1–13 (2018)
 49. S. Acharya, J. Mondal, S. Ghosh, S.K. Roy, P.K. Chakrabarti, Multiferroic behaviour of Lanthanum ortho ferrite (LaFeO₃). *Mater. Lett.* **64**, 415–418 (2010)
 50. L. Vaisman, H.D. Wagner, G. Marom, The role of surfactants in dispersion of carbon nanotubes. *Adv. Coll. Interface. Sci.* **128–130**, 37–46 (2006)
 51. M. Zhang, Y. Wang, H. Liu, T. Ma, J. Xie, S. Shao, Controllable synthesis of CoNb₂O₆ nanoparticles on multifunctional sulfur and phosphorus dual-doped graphene as advanced electrodes for hybrid supercapacitors. *Electrochim. Acta* **309**, 104–115 (2019)
 52. Z. Li, J. Wang, S. Liu, X. Liu, S. Yang, Synthesis of hydrothermally reduced Graphene/MnO₂ composites and their electrochemical properties as supercapacitors. *J. Power Sources* **196**, 8160–8165 (2011)
 53. K. Hareesh, B. Shateesh, J.F. Williams, K. Asokan, D.M. Phase, K. Priya Madhuri, S.K. Haram, S.D. Dhole, Enhanced supercapacitance behaviour of low energy ion beam reduced graphene oxide. *Mater. Res. Express* **4**, 065018 (2017)
 54. D.M.G.T. Nathan, S.J.M. Boby, P. Basu, R. Mahesh, S. Harish, S. Joseph, P. Sahayaraj, One-pot hydrothermal preparation of Cu₂O-CuO/rGO nanocomposites with enhanced electrochemical performance for supercapacitor applications. *Appl. Surf. Sci.* **449**, 474–484 (2018)
 55. K. Siwatch, K. Sharma, A. Arora, S.K. Tripathi, Review of supercapacitors: materials and devices. *J. Energy Storage* **21**, 801–825 (2019)
 56. R. Kumar, H.-J. Kim, S. Park, A. Srivastava, I.-K. Oh, Graphene-wrapped and cobalt oxide-intercalated hybrid for extremely durable super-capacitor with ultrahigh energy and power densities. *Carbon* **79**, 192–202 (2014)
 57. R. Kumar, R. Matsuo, K. Kishida, M.M. Abdel-Galeil, Y. Suda, A. Matsuda, Homogeneous reduced graphene oxide supported NiO-MnO₂ ternary hybrids for electrode material with improved capacitive performance. *Electrochim. Acta* **303**, 246–256 (2019)
 58. R. Kumar, R.K. Singh, A.R. Vaz, R. Savu, S.A. Moshkalev, Self-assembled and one-step synthesis of interconnected 3D network of Fe₃O₄/reduced graphene oxide nanosheets hybrid

- for high-performance supercapacitor electrode. *ACS Appl. Mater. Interfaces* **9**, 8880–8890 (2017)
59. S. Maiti, A.K. Das, S.K. Karan, B.B. Khatua, Carbon nano-horn-graphene nanoplate hybrid: an excellent electrode material for supercapacitor application. *J. Appl. Polym. Sci.* **132**, 42118–42124 (2015)

Publisher's Note Springer Nature remains neutral with regard to jurisdictional claims in published maps and institutional affiliations.